

Context-Guided Semantic Alignment for Feature Fusion Networks

Hyungseop Lee[✉], Jiho Lee[✉], and Woochul Kang^{*✉}

Department of Embedded Systems Engineering, Incheon National University,
Yeonsu-gu 22012, South Korea
{hsss0927, wchkang}@inu.ac.kr

Abstract. Feature fusion networks are fundamental components in modern object detectors, aggregating multi-scale features to detect objects of varying sizes. However, directly fusing features from different pyramid levels often introduces semantic inconsistency due to their heterogeneous representations. In this paper, we propose Feature Interaction Network (FINE), a lightweight semantic alignment module that refines low-level features via high-level contextual guidance using cross-level attention prior to fusion. To bridge the structural gap and ensure computational efficiency, we introduce an Alignment-Aware Token Sampling that aligns corresponding spatial regions across scales, reducing the attention complexity by an order of magnitude. The resulting attention weights generate a spatial-channel modulation map that is upsampled and applied to the low-level features via residual element-wise modulation. This mechanism ensures that the network selectively enhances semantically relevant pixels while preserving the sub-pixel localization accuracy necessary for dense prediction tasks. FINE is generally applicable to various detectors and consistently improves detection accuracy without compromising efficiency.

1 Introduction

Modern object detectors [1, 19, 49, 53, 55, 58] generally follow a tripartite architecture, consisting of a backbone for feature extraction, a neck for feature fusion, and a head for prediction, as illustrated in Figure 1(a). The backbone extracts hierarchical representations from the input image, where early layers capture fine-grained local details with small receptive fields, while deeper layers produce semantically rich but spatially coarse representations due to progressively expanded receptive fields. To exploit complementary information across feature levels, the neck aggregates these pyramidal features via cross-level fusion, and the fused representations are fed into the head for bounding box regression and category classification. As an intermediate component bridging feature extraction and final prediction, the neck is responsible for constructing multi-scale representations essential for detecting objects of varying sizes.

* Corresponding author.

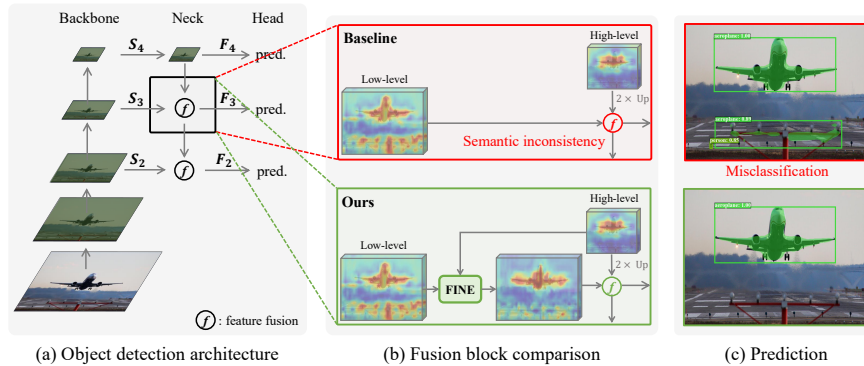


Fig. 1: Semantic inconsistency in conventional feature fusion. (a) Modern detectors use a neck to aggregate multi-scale backbone features. (b) Standard fusion blocks combine features via naive element-wise operations, enforcing pixel-wise alignment but leaving representational discrepancies unresolved. In contrast, our method mitigates this by explicitly aligning low-level features with high-level context prior to fusion. (c) In baseline models, semantic inconsistency often causes misclassifications in background clutter. FINE reduces such errors and improves detection reliability.

Despite the widespread adoption of feature fusion networks [10, 31, 35, 47], existing approaches often overlook a critical issue: *semantic inconsistency* between feature levels. In typical feature pyramid architectures, high-level features learn rich semantic contexts while losing spatial information due to repeated downsampling in the backbone network. In contrast, low-level features preserve spatial details but lack sufficient semantic abstraction. Directly fusing these heterogeneous features through naive element-wise operations, such as addition or concatenation, enforces position-wise aggregation without resolving the underlying representational discrepancies, as illustrated by the activation heatmaps in Figure 1(b). This semantic mismatch induces information conflicts [16] at corresponding spatial positions, thereby distorting the fused representation and increasing the risk of inaccurate classification in background clutter, as shown in Figure 1(c) (detailed analysis in Section 5.4).

Motivated by these limitations, we propose a lightweight semantic alignment module, termed **F**eature **I**nteraction **N**etwork (FINE). Before feature fusion, FINE performs spatial-channel modulation on low-level features, guided by the rich context of their corresponding higher-level representations. To generate this modulation map, we employ multi-head cross-level attention to capture diverse semantic interactions. However, directly enforcing dense pixel-to-pixel interactions across pyramid levels is not only computationally prohibitive but also inherently unaligned in terms of effective receptive fields. Specifically, features from different backbone stages encode distinct contextual scales and exhibit inconsistent receptive field sizes, making naive position-wise interactions unreliable for establishing meaningful cross-level correspondences. To address this, we introduce Alignment-Aware Token Sampling (AATS), which condenses features into

representative tokens while aligning their effective receptive fields across levels. Based on these aligned and reduced tokens, our bottleneck cross-level attention establishes robust correspondences to selectively inject high-level semantic context into low-level features. Since the modulation map is estimated at a coarse regional scale due to token sampling, we adopt a residual modulation strategy to preserve high-resolution spatial cues critical for accurate object localization.

Extensive experiments on the MS COCO [33] dataset demonstrate that FINE consistently boosts performance across various detection architectures with negligible computational overhead. These gains are largely driven by a reduction in false positives, suppressing the misclassification of background clutter as foreground objects. Furthermore, FINE yields notable gains for small object detection by enriching the limited semantic context of low-level features. While our evaluation primarily focuses on object detection, FINE generalizes well to other datasets and can be readily integrated into other dense prediction tasks (*e.g.*, segmentation), as detailed in Appendix Section D

Our contributions can be summarized as follows:

- We propose FINE, a lightweight plug-and-play module that facilitates efficient inter-level cross-scale attention to mitigate semantic misalignment across feature pyramid levels in real-time detectors.
- We propose Alignment-Aware Token Sampling, a mechanism that significantly reduces the computational overhead of cross-level attention while establishing precise regional correspondences across pyramidal feature levels.
- Extensive evaluations demonstrate that FINE consistently enhances detection performance across diverse architectures with minimal inference overhead. By mitigating semantic conflicts, FINE substantially reduces false positives and yields significant improvements in small object detection.

2 Related Work

2.1 Misalignment in Feature Fusion Networks

Semantic misalignment across pyramid levels poses a fundamental challenge in feature fusion networks. To alleviate this issue, several approaches recalibrate channel-wise feature responses. For example, Squeeze-and-Excitation (SENet) [15] is widely used to modulate channel importance. Building on this, FaPN [18] adds a feature selection module to emphasize informative channels, and AFF [7] extends SENet by incorporating multi-scale pooling for both global and local context. AugFPN [12] further mitigates semantic gaps by enforcing consistent supervision across all pyramid levels. Other works redesign the fusion architecture itself: for instance, A^2 -FPN [16] aggregates global context from multiple levels to reduce semantic loss, and CATFPN [17] refines separate feature pyramids using global context blocks. In parallel, some studies address pixel-level misalignment caused by artifacts from naive upsampling, employing learnable sampling offsets [18, 21, 38, 54] or soft upsampling [11, 29] to preserve fine-grained

textures. These approaches can improve fusion quality but often introduce significant computational overhead or lack plug-and-play applicability to existing detectors.

2.2 Attention Mechanisms for Object Recognition

Self-attention [52] has been widely adopted to model long-range dependencies. However, its quadratic complexity [8] has motivated numerous efficient variants, including local attention [20, 36, 49, 53], hybrid CNN–transformer architectures [40, 56], kernel-based linear attention [3, 26, 37], and token sparsification [2, 30, 44]. Despite their efficacy, these mechanisms are tailored for intra-level feature extraction within a single scale.

Several studies have leveraged cross-attention to model dependencies across heterogeneous feature representations. For multi-scale feature fusion, FPT [57] introduces transformer-style interactions across the feature pyramid, while CLASS [48] employs cross-level attention in a U-Net-based [46] architecture for salient object detection. However, their dense pixel-wise computations introduce substantial latency, limiting their applicability to real-time architectures. While the DETR family [4, 28, 34, 59] and its real-time variants [19, 43, 55, 58] successfully employ cross-attention for generic object detection, this mechanism is primarily used in the detection head for object query decoding, rather than for cross-level feature fusion. Consequently, efficient cross-level attention within feature fusion networks remains largely unexplored in real-time object detection, hindered by the prohibitive computational costs of high-resolution features and the spatial-channel heterogeneity.

3 Preliminaries

In this section, we briefly review Feature Pyramid Networks (FPN) [31] and establish the notation used throughout this paper. Given an input image, a backbone network extracts a hierarchy of feature maps $\{S_2, S_3, S_4\}$, where each $S_l \in \mathbb{R}^{H_l \times W_l \times C_l}$ corresponds to strides of $\{8, 16, 32\}$ pixels relative to the input image, respectively. Each S_l is first projected to a unified channel dimension C via 1×1 convolutions. At the l -th fusion stage, the low-level and high-level features are defined as:

$$F_{\text{low}} = \text{Conv}_{1 \times 1}(S_l), \quad F_{\text{high}} = \text{Conv}_{1 \times 1}(S_{l+1}). \quad (1)$$

These adjacent features are integrated using a top-down pathway:

$$F_{\text{fused}} = f(F_{\text{low}}, \text{Up}(F_{\text{high}}, \text{scale} = 2)), \quad (2)$$

where $\text{Up}(\cdot)$ denotes nearest-neighbor interpolation and $f(\cdot)$ represents a fusion operator, such as element-wise addition or concatenation. The resulting F_{fused} subsequently serves as the high-level input for the next fusion stage

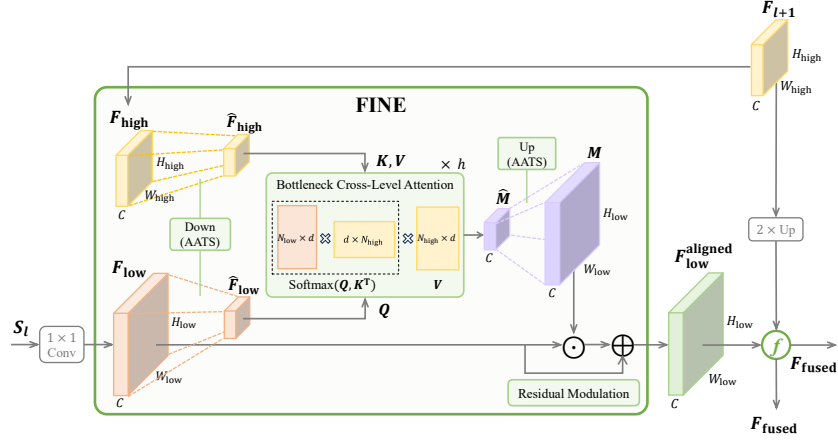


Fig. 2: Overview of the Feature Interaction Network (FINE). Given adjacent low- and high-level features (F_{low} and F_{high}), FINE refines F_{low} into a semantically aligned representation $F_{low}^{aligned}$ under the guidance of F_{high} . Through Alignment-Aware Token Sampling (AATS), F_{low} is condensed into \hat{F}_{low} as the Query (Q), and F_{high} is compressed into \hat{F}_{high} as the Key (K) and Value (V), with an alignment factor that explicitly aligns their regional correspondence. The resulting bottleneck cross-level attention produces a spatial-channel modulation map \hat{M} . After upsampling, the map is applied to F_{low} via element-wise multiplication, followed by a residual connection to preserve fine-grained localization cues.

($l - 1$). Through this recursive process, the network constructs multi-scale features $\{F_2, F_3, F_4\}$, integrating fine-grained spatial details with high-level semantic information. These features may be further refined by an additional pathway [35] or fed directly into the detection head.

4 Method

4.1 Overview

Figure 2 illustrates an overview of our Feature Interaction Network (FINE). We reformulate the standard fusion process Eq. 2 by replacing the original low-level feature F_{low} with its semantically aligned representation $F_{low}^{aligned}$, conditioned on the high-level context F_{high} :

$$F_{fused} = f(F_{low}^{aligned}, \text{Up}(F_{high}, \text{scale}=2)), \quad (3)$$

where $F_{low}^{aligned} = \text{FINE}(F_{low}, F_{high})$.

To generate $F_{low}^{aligned}$, the FINE module employs three key components: (i) Alignment-Aware Token Sampling (Section 4.2) to align inherently unaligned effective receptive fields and reduce memory and computational cost, (ii) Bottleneck Multi-Head Cross-Level Attention (Section 4.3) to construct a spatial-channel modulation map that captures diverse cross-level semantic interactions

across multiple subspaces, and (iii) Residual Spatial-Channel Modulation (Section 4.4) to apply the estimated modulation, selectively injecting high-level context into low-level features while preserving fine spatial details.

4.2 Alignment-Aware Token Sampling

To alleviate semantic inconsistency across adjacent pyramid levels, we employ cross-level attention to refine the low-level feature F_{low} under the semantic guidance of the high-level feature F_{high} . However, as illustrated in Figure 3(a), vanilla dense pixel-to-pixel interaction faces a fundamental limitation in pyramidal architectures: features from adjacent backbone stages inherently possess different effective receptive fields (ERFs) [39], *i.e.*, the spatial region of the input image that influences each token’s representation. Since F_{high} is extracted at a spatial stride r times larger than that of F_{low} ($r > 1$, typically $r = 2$), pixels from different stages correspond to inconsistent physical regions of the input image. When these misaligned pixels are directly treated as tokens for cross-level attention, this coverage mismatch prevents reliable correspondence between features at different contextual scales.

Furthermore, the massive token count in high-resolution visual features makes the vanilla approach computationally prohibitive for real-time applications. While lightweight variants such as window- [36] or area-based schemes [49], as depicted in Figure 3(c,d), improve efficiency by restricting attention to local regions, they limit the long-range dependencies of F_{high} and fail to align the ERFs.

To establish ERF alignment and mitigate the excessive token density, we introduce an *Alignment-Aware Token Sampling* (AATS) strategy that constructs compact, ERF-aligned token representations prior to cross-level attention. AATS downsamples both feature levels while accounting for their stride discrepancy, using asymmetric sampling kernels to align their effective receptive fields:

$$\begin{aligned}\hat{F}_{\text{high}} &= \text{Down}(F_{\text{high}}, \text{kernel} = k), \\ \hat{F}_{\text{low}} &= \text{Down}(F_{\text{low}}, \text{kernel} = rk)\end{aligned}\tag{4}$$

where k is the base sampling kernel size for the high-level feature, and r is the *alignment-aware sampling ratio*.

Assuming non-overlapping pooling, the resulting features are $\hat{F}_{\text{high}} \in \mathbb{R}^{\frac{H_{\text{high}}}{k} \times \frac{W_{\text{high}}}{k} \times C}$ and $\hat{F}_{\text{low}} \in \mathbb{R}^{\frac{H_{\text{low}}}{rk} \times \frac{W_{\text{low}}}{rk} \times C}$. Since the choice of pooling operator has marginal impact on cross-level attention quality, we adopt parameter-free average pooling as our default implementation of AATS (see Appendix Section B for an ablation study).

For all object detectors in the evaluation, we set the sampling ratio $r = 2$ to match the downsampling ratio between adjacent backbone stages. Empirical validation of this choice is provided in Section 5.3, and a theoretical rationale in terms of ERF alignment is given in Appendix Section F.

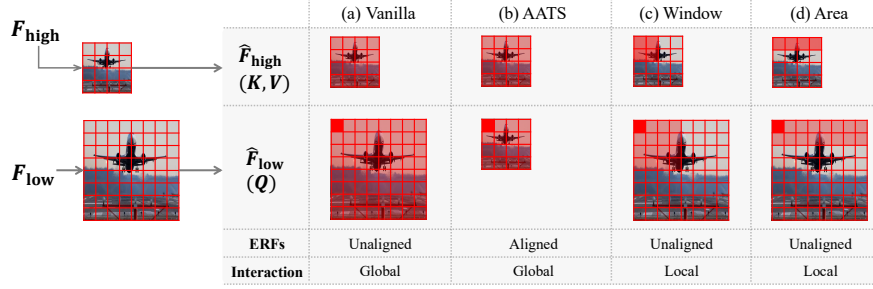


Fig. 3: Visualization of Effective Receptive Fields (ERFs) and token dependencies. Each grid cell represents the ERF of a token with respect to the input image. Shaded grids indicate tokens participating in attention, where the solid red square denotes the query token. **(a)** In the vanilla mechanism, tokens across adjacent pyramid stages exhibit inherently unaligned ERFs due to varying backbone strides. **(b)** Alignment-Aware Token Sampling (AATS) synchronizes ERFs across levels, establishing reliable cross-level correspondences for accurate global interaction. Local attention variants including **(c)** window and **(d)** area attention restrict long-range dependencies and leave the ERFs unaligned.

4.3 Bottleneck Multi-Head Cross-Level Attention

Given the ERF-aligned, condensed feature maps \hat{F}_{low} and \hat{F}_{high} from AATS, we apply multi-head cross-level attention in a bottleneck manner to generate a spatial-channel modulation map M . By assigning \hat{F}_{low} as the query and \hat{F}_{high} as the key and value, each spatial location in \hat{F}_{low} selectively retrieves semantically relevant contextual information from higher-level representations. The condensed maps are flattened and linearly projected to obtain queries (Q), keys (K), and values (V):

$$Q = \text{Flatten}(\hat{F}_{\text{low}})W_Q, \quad K = \text{Flatten}(\hat{F}_{\text{high}})W_K, \quad V = \text{Flatten}(\hat{F}_{\text{high}})W_V, \quad (5)$$

where $W_Q, W_K, W_V \in \mathbb{R}^{C \times C}$ are learnable projection weights. This yields $Q \in \mathbb{R}^{N_{\text{low}} \times C}$ and $K, V \in \mathbb{R}^{N_{\text{high}} \times C}$, with reduced sequence lengths $N_{\text{low}} = \frac{H_{\text{low}}W_{\text{low}}}{r^2k^2}$ and $N_{\text{high}} = \frac{H_{\text{high}}W_{\text{high}}}{k^2}$.

To capture diverse semantic-spatial interactions across heterogeneous feature levels, we adopt multi-head attention. By projecting Q , K , and V into h independent subspaces (each with dimension $d = C/h$), the network jointly captures cross-level correlations from multiple representation perspectives rather than a single shared space. Formally, for the i -th head, the cross-level attention is computed as:

$$\text{head}_i = \text{Softmax}\left(\frac{Q_i K_i^\top}{\sqrt{d}}\right) V_i \in \mathbb{R}^{N_{\text{low}} \times d}, \quad (6)$$

where the attention weights identify cross-level token correspondences, and V_i carries the high-level semantic content to be selectively injected into each low-level spatial location. The outputs from all heads are concatenated, projected,

and reshaped into a spatial feature map \hat{M} :

$$\hat{M} = \text{Reshape}\left(\text{Concat}(\text{head}_1, \dots, \text{head}_h)W^O\right) \in \mathbb{R}^{\frac{H_{\text{low}}}{rk} \times \frac{W_{\text{low}}}{rk} \times C}, \quad (7)$$

where $W^O \in \mathbb{R}^{C \times C}$ is a learnable projection matrix. Finally, \hat{M} is spatially upsampled by a factor of rk to recover the original resolution of F_{low} :

$$M = \text{Up}(\hat{M}, \text{scale}=rk) \in \mathbb{R}^{H_{\text{low}} \times W_{\text{low}} \times C}. \quad (8)$$

This upsampling broadcasts the encoded semantic context across $rk \times rk$ local regions, providing spatially aligned guidance for subsequent modulation (Section 4.4).

4.4 Residual Spatial-Channel Modulation

Instead of directly using the upsampled attention output M as a standalone feature, we utilize it to refine the original low-level feature F_{low} . Because M is estimated from condensed tokens via AATS, it remains spatially coarser than the dense, raw feature map. Consequently, completely replacing F_{low} with M would inevitably discard the high-resolution, fine-grained details essential for precise dense prediction. To address this, we treat M as a spatial-channel modulation map that adaptively re-weights F_{low} rather than overwriting it. Unlike conventional channel-attention frameworks that apply a single global scaling factor per channel, M provides location-specific modulation across both spatial and channel dimensions, allowing the network to selectively emphasize object-relevant regions while suppressing background noise.

However, direct modulation ($F_{\text{low}}^{\text{aligned}} = F_{\text{low}} \odot M$) tightly couples the refined features to the coarse spatial structure inherited from the bottleneck attention, which may attenuate fine-grained spatial details. To provide a more conservative refinement pathway, we formulate the modulation as a residual transformation:

$$F_{\text{low}}^{\text{aligned}} = (F_{\text{low}} \odot M) + F_{\text{low}}, \quad (9)$$

where \odot denotes element-wise multiplication. The identity mapping ($+F_{\text{low}}$) provides a direct information pathway, preserving the original high-resolution spatial details. The modulation term ($F_{\text{low}} \odot M$) functions as a data-dependent residual transformation that adaptively rescales feature responses based on high-level contextual cues.

5 Experiments

5.1 Experimental Setup

We conduct experiments on MS COCO dataset [33], which consists of 118k training images and 5k validation images. Following standard practice, we evaluate object detection performance using official COCO metrics: mean Average Precision (AP). For fair comparison, FINE is plugged into each baseline without

Model	Fusion Method	#Params	FLOPs	FPS	AP _{50:95}	AP ₅₀	AP _s	AP _m	AP _l
SOTA Real-Time Object Detectors									
RT-DETRv1 R18 [58]	H-Enc	20.2M	61.7G	80	46.5	63.8	28.4	49.8	63.0
RT-DETRv1 R50* [58]	H-Enc	42.9M	138.0G	40	52.8	71.0	34.2	57.3	70.0
YOLOv8-S [23]	PAN	11.2M	28.6G	189	45.0	61.8	26.0	49.9	61.0
YOLOv10-S [53]	PAN	8.1M	24.8G	173	46.2	63.0	26.9	51.1	63.7
YOLOv12-S [49]	PAN	9.1M	19.4G	112	47.6	64.5	28.3	52.7	65.9
RT-DETRv1 R18	H-Enc + FINE	21.2M	62.9G	78	47.3 (+0.8)	64.4	30.1	50.8	63.5
RT-DETRv1 R50	H-Enc + FINE	44.0M	139.2G	40	53.3 (+0.5)	71.3	35.6	57.6	70.4
YOLOv8-S	PAN + FINE	12.3M	29.6G	177	45.8 (+0.8)	62.7	27.0	51.2	62.1
YOLOv10-S	PAN + FINE	9.0M	25.7G	153	46.7 (+0.5)	63.6	28.2	51.4	63.2
YOLOv12-S	PAN + FINE	10.5M	21.2G	106	48.2 (+0.6)	65.1	30.6	53.3	65.2
Classic Object Detectors									
Faster R-CNN R50 [45]	FPN	41.8M	134.4G	-	37.0	58.5	21.1	40.3	48.2
RetinaNet R50 [32]	FPN	34.0M	151.5G	-	36.4	55.7	19.1	40.0	48.9
FCOS R50 [50]	FPN	32.3M	128.2G	-	39.2	58.2	22.1	42.4	51.3
Faster R-CNN R50	FPN + FINE	42.8M	135.5G	-	39.1 (+2.1)	60.8	23.3	42.6	50.4
RetinaNet R50	FPN + FINE	35.0M	152.9G	-	37.3 (+0.9)	56.8	20.6	40.7	49.4
FCOS R50	FPN + FINE	33.3M	129.6G	-	39.8 (+0.6)	58.7	23.3	43.1	51.2

Table 1: Performance of the proposed FINE module on various detectors on COCO val2017. Models with ‘*’ mark yield slightly lower performance compared to the results reported in the original paper [58], which may stem from differences in experimental setup or unreleased training details. PAN: PANet-style Fusion Network. H-Enc: Hybrid Encoder.

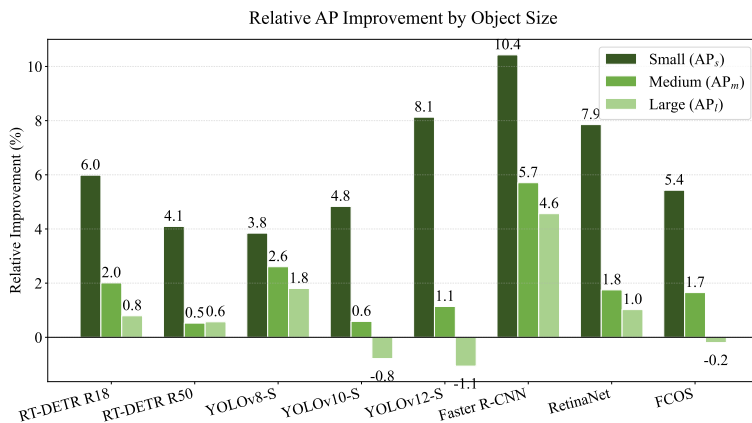


Fig. 4: Relative AP improvement across different object sizes. The proposed FINE module achieves the most significant gains in small object detection.

any modification to the original training recipes. To evaluate efficiency under resource constraints, FPS and latency are measured on an NVIDIA Jetson Orin Nano with TensorRT v10.7.0 [42].

5.2 Main Results

Performance on Various Detectors To validate the generality of our approach, we integrate FINE into a diverse range of detectors, as summarized in Table 1. For CNN-based one-stage real-time detectors such as YOLOv8-S [23], FINE improves AP from 45.0 to 45.8 with negligible overhead (+1.0G FLOPs, +1.1M parameters). We also evaluate FINE on RT-DETR-R50 [58], an end-to-end transformer-based detector that replaces post-processing with a hybrid encoder-decoder architecture. When inserted into the hybrid encoder, FINE increases AP from 52.8 to 53.3 while fully maintaining the real-time throughput of 40 FPS. Lastly, on the attention-centric real-time detector YOLOv12-S [49], FINE yields a steady improvement from 47.6 to 48.1 AP. These consistent results demonstrate that FINE provides reliable, architecture-agnostic improvements.

While FINE improves detection accuracy across most object scales, the gains are particularly pronounced for small objects, as shown in Figure 4. By mitigating the semantic inconsistency overlooked in early fusion architectures such as FPN [31], FINE achieves substantial relative improvements in AP_s : 10.4% for Faster R-CNN [45], 7.9% for RetinaNet [32], and 5.4% for FCOS [50]. FINE also consistently improves small object detection in modern detectors with advanced fusion schemes, including PANet [35] and Hybrid Encoder [58], yielding AP_s gains of 6.0% on RT-DETR R18 [58], 4.8% on YOLO v10-S [53], and 8.1% on YOLOv12-S [49]. While we observe marginal fluctuations in AP_l for some models, such as YOLOv12-S, these likely reflect statistical noise rather than meaningful architectural degradation, particularly as large object detection accuracy in modern detectors is already near saturation. We further validate FINE on the VisDrone-DET2019 [9] dataset, a benchmark dominated by small objects, in Appendix Section E.

Comparison with Prior Cross-Scale Feature Alignment Methods We compare FINE against representative feature alignment methods on two distinct detector architectures: Faster R-CNN R50 [45] and RT-DETR R18 [58]. As shown in Table 2, FINE achieves the best accuracy-efficiency trade-off in both cases. On Faster R-CNN R50, FINE improves AP from 37.0 to 39.1 with only +1.0M parameters and +1.1G FLOPs. In contrast, MGC [16] consumes +27.4G FLOPs for a smaller +1.3 AP gain, as its global context aggregation and redistribution across all pyramid levels introduce substantial computational overhead. Furthermore, FINE achieves competitive accuracy while requiring substantially fewer resources than FaPN [18] and AdaFPN [54], which add +9.2G and +25.0G FLOPs, respectively. A similar trend is observed on RT-DETR R18. While several prior methods bring marginal or even negative changes, such as SNI [29] and AdaFPN [54], degrading the baseline by 0.2 and 0.4 AP, respectively, FINE achieves the largest improvement from 38.7 to 39.7 AP with minimal overhead (+1.0M parameters, +1.2G FLOPs). These results demonstrate that resolving semantic misalignment through lightweight cross-level attention is more efficient and robust than heavier architectural modifications or sampling-based strategies.

Faster R-CNN R50 [45]				RT-DETR R18 [58]			
Fusion Method	#Params	FLOPs	Δ AP	Fusion Method	#Params	FLOPs	Δ AP
baseline	41.8M	134.4G	-	baseline	20.2M	61.7G	-
+ SNI* [29]	41.8M	134.4G	37.0 \rightarrow 37.7	+ SNI* [29]	20.2M	61.7G	38.7 \rightarrow 38.5
+ FaPN [18]	48.5M	143.6G	37.9 \rightarrow 39.2	+ FaPN* [18]	21.9M	71.8G	38.7 \rightarrow 39.0
+ AdaFPN [54]	45.6M	159.4G	37.8 \rightarrow 39.0	+ AdaFPN* [54]	22.9M	82.8G	38.7 \rightarrow 38.3
+ A^2 -FPN(MGC)* [16]	44.4M	161.8G	37.0 \rightarrow 38.3	+ A^2 -FPN(MGC)* [16]	21.1M	68.7G	38.7 \rightarrow 38.6
+ FINE	42.8M	135.5G	37.0 \rightarrow 39.1	+ FINE	21.2M	62.9G	38.7 \rightarrow 39.7

Table 2: Comparison with prior alignment methods. Methods with ‘*’ are re-implemented and trained either according to the original paper or a Torchvision reference recipe [51]. ‘MGC’ denotes the use of only the Multi-level Global Context module from A^2 -FPN.

Model	Attention	Complexity	#Params	FLOPs	Mem (MB)	FPS	Latency	AP
RT-DETR R18	-	-	20.2M	61.74G	64.50	80	12.81ms	38.7
+ FINE	Vanilla [52]	$O(H_{low}W_{low} \times H_{high}W_{high})$	+1.0M	+18.0G	+1223.48	57	17.74ms	39.5
	Window [36]	$O(H_{low}W_{low}M^2)$		+8.9G	+65.11	68	15.05ms	39.7
	Area [49]	$O(\frac{H_{low}W_{low} \times H_{high}W_{high}}{A})$		+10.0G	+65.67	69	14.71ms	39.2
	Linear [26]	$O(H_{low}W_{low} + H_{high}W_{high})$		+7.0G	+18.42	64	16.05ms	39.0
	AATS	$O(\frac{H_{low}W_{low}}{r \times k^2} \times \frac{H_{high}W_{high}}{k^2})$		+1.2G	+1.17	78	13.24ms	39.7

Table 3: Performance of various attention strategies integrated into the FINE module, evaluated on RT-DETR R18 (1 \times schedule). Window attention uses a window size of 7×7 ($M = 7$) [36], and area attention divides feature maps into four regions ($A = 4$) [49].

5.3 Ablation Study

We ablate the four core design choices of FINE on RT-DETR R18 [58] and Faster R-CNN R50 [45] under a 1 \times training schedule to assess the contribution of each component in FINE. Specifically, we investigate the attention strategy, the alignment-aware sampling ratio, the number of attention heads, and the modulation design.

Cross-level Attention Strategy We evaluate several attention variants within FINE on RT-DETR R18 [58]. As reported in Table 3, vanilla attention [52] incurs prohibitive quadratic overhead (+18.0G FLOPs, +1223.48 MB memory), reducing FPS from 80 to 57, while its performance gain remains limited due to unaligned cross-level ERFs (38.7 \rightarrow 39.5 AP). Local attention variants such as window [36] and area [49] reduce some computational cost, but still introduce noticeable overhead (+8.9G to +10.0G FLOPs, +65.11 to +65.67 MB memory) while restricting long-range dependencies. Linear attention [26] further improves efficiency through kernel approximation, yet processing high-resolution features still incurs considerable overhead (+7.0G FLOPs, +18.42 MB memory). Since these methods are primarily designed for intra-level interactions, they

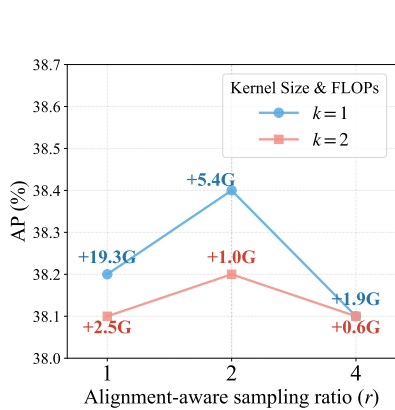


Fig. 5: Ablation on AATS sampling ratio r . Aligning r with the backbone’s stride ($r = 2$) provides the best performance-efficiency trade-off.

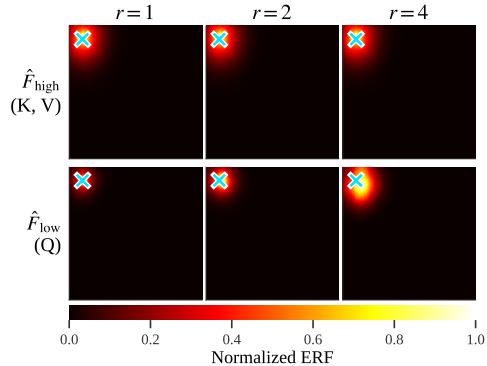


Fig. 6: Visualization of ERFs across different sampling ratios r . The cyan ‘X’ denotes the target token, selected at a normalized spatial coordinate of (0.1,0.1) to ensure the exact same physical anchor point on the input image regardless of the feature map resolutions.

fail to address the underlying structural misalignment across levels. In contrast, Alignment-Aware Token Sampling (AATS) explicitly synchronizes ERF scales before attention, achieving the best accuracy (39.7 AP) with negligible overhead (+1.2G FLOPs, +1.17 MB memory). Compared with vanilla attention, AATS reduces computational and memory costs by 93.3% and 99.9%, respectively, while largely preserving real-time speed (80 \rightarrow 78 FPS).

Alignment-Aware Sampling Ratio The core hyperparameter of AATS is the alignment-aware sampling ratio r , which controls the degree to which the ERFs of \hat{F}_{low} and \hat{F}_{high} are synchronized. Figure 5 reports AP and FLOPs overhead on Faster R-CNN R50 [45] for $r \in \{1, 2, 4\}$ and two kernel sizes $k \in \{1, 2\}$. While $r = 4$ incurs the least overhead (+1.9G for $k = 1$; +0.6G for $k = 2$), it yields lower accuracy than $r = 2$, dropping from 38.4% to 38.1% AP for $k = 1$, and from 38.2% to 38.1% AP for $k = 2$. Conversely, $r = 1$ introduces heavy computational costs (+19.3G for $k = 1$; +2.5G for $k = 2$) with no accuracy benefits (38.2% and 38.1% AP, respectively). Setting $r = 2$ thus achieves the best accuracy-efficiency trade-off across both kernel sizes.

Figure 6 provides an ERF [39] visualization that explains this result. For each cell, the ERF of a target token, marked by the cyan ‘X’ at the normalized coordinate (0.1, 0.1), is computed by back-propagating the token’s response to the input image and rendered as a heatmap (brighter colors indicate stronger contribution). The normalized anchor keeps the physical reference consistent across resolutions, so comparing the two rows within each column reveals whether the ERFs are aligned at that r . When $r = 1$, the sampled low-level tokens span a

Metric	Baseline (w/o FINE)	Number of Heads (h) in FINE, given $C = 256$						
		1	4	8	16	32	64	128
Per-Head Dim (d)	-	256	64	32	16	8	4	2
AP	37.0	37.9	38.1	38.1	38.2	38.2	38.1	38.0

Table 4: Ablation on the number of attention heads h . Evaluated on Faster R-CNN R50 with COCO val2017 ($1 \times$ schedule). With the total channel dimension fixed to $C = 256$, varying h reveals the trade-off between subspace diversity and per-head representational capacity.

smaller physical footprint than the high-level tokens, causing a scale mismatch. In contrast, $r = 4$ over-expands the low-level receptive field beyond the target region covered by the high-level tokens. Only at $r = 2$ do the ERFs of the two layers align closely, with the sampled tokens covering comparable physical regions around the anchor point and enabling reliable regional correspondences. Together with the ERF-size analysis in Appendix Section F, this provides both theoretical and empirical justification for choosing $r = 2$. Guided by these observations and prioritizing a lightweight design, we set $k = 1$ for the $l = 3$ fusion stage and $k = 2$ for the $l = 2$ fusion stage.

Number of Attention Heads To investigate the multi-head mechanism within FINE, we ablate the number of attention heads h on Faster R-CNN R50 with a fixed channel dimension $C = 256$. This ablation aims to analyze the fundamental trade-off between maximizing subspace diversity for cross-level interactions and preserving sufficient per-head representational capacity. As reported in Table 4, performance peaks at 38.2% AP when $h = 16$ or $h = 32$, where each head operates at a dimension of $d = 16$ or $d = 8$, respectively. With fewer heads, such as $h = 1$ or $h = 4$, the limited number of shared subspaces restricts the diversity of cross-level interactions, yielding 37.9% AP and 38.1% AP, respectively. Conversely, increasing h beyond 32 reduces the per-head dimension below 8, which compresses the representational capacity of each subspace and degrades performance (e.g., dropping to 38.0% AP at $h = 128$). Based on this analysis, we fix the per-head dimension to $d = 16$ as our default setting by adjusting h accordingly.

Residual Modulation We ablate the two design choices introduced in Section 4.4 on RT-DETR R18: (i) whether to use the cross-level attention output as a direct refined feature or as a modulation map for F_{low} , and (ii) whether to apply that modulation directly ($F_{\text{low}} \odot M$) or through the residual formulation (Eq. 9). Figure 7 reports the L_1 loss, GIoU training loss, and small object Average Precision (AP_S) across the four configurations. Using the attention output directly as a refined feature (No modulation) yields substantially higher localization losses and drops AP_S from 21.4 (baseline) to 15.4, confirming that the spatially coarse signal produced under bottleneck attention cannot replace the

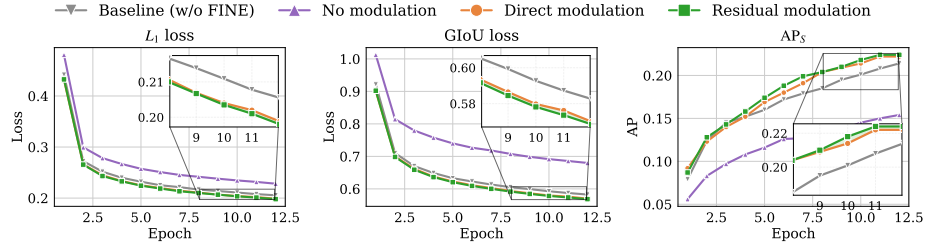


Fig. 7: Ablation of the modulation strategy on localization losses and small object detection. Training curves for RT-DETR R18 on COCO train2017 (1× schedule). No modulation underperforms even the FINE-free baseline on both metrics, whereas repurposing the attention output as a modulation map (Direct and Residual) consistently improves localization learning and AP_S. The Residual variant maintains marginally lower losses and higher AP_S than Direct modulation throughout training (zoomed insets).

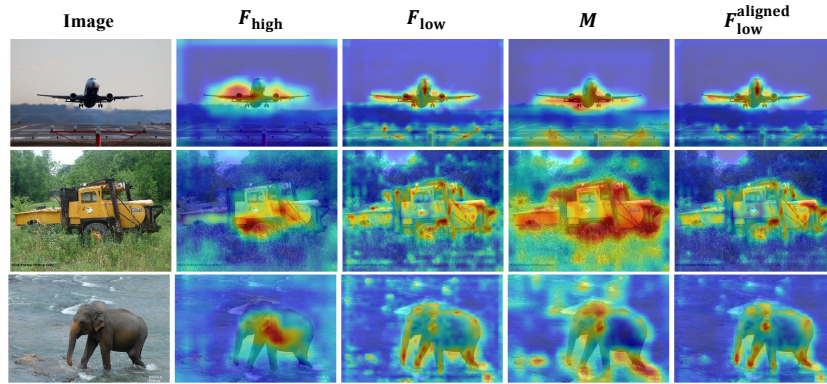


Fig. 8: Activation heatmaps of high-level, low-level, learned modulation map, and aligned low-level features, visualized at the $l = 3$ fusion stage on COCO.

high-resolution F_{low} . Once the attention output is repurposed as a modulation map, both direct and residual modulation reduce the losses and improve AP_S beyond the baseline, reaching 22.2 and 22.4 respectively. We attribute the consistent advantage of the residual variant to its design: while direct modulation rescales every pixel of F_{low} by the spatially coarse map M and thus inevitably attenuates fine-grained spatial cues, the residual formulation preserves the original high-resolution representation intact and treats modulation as an additive refinement. Such preservation of sub-pixel localization cues is particularly critical for small objects, whose limited spatial extent leaves little redundancy to absorb any loss of fine-grained detail.

	#Images	#TPs (↑)	#FPs (↓)	#FNs (↓)	Precision	Recall	F1-score
w/o FINE	5,000	23,833	21,557	12,502	0.525	0.656	0.583
w/ FINE	5,000	24,186	19,417	12,149	0.555	0.666	0.605
Improvement	-	+1.48%	-9.93%	-2.82%	+5.71%	+1.52%	+3.77%

Table 5: Detection error analysis of Mask R-CNN R50 on COCO val2017. Results are computed with an IoU threshold of 0.5 and confidence threshold of 0.5.



Fig. 9: False positive suppression comparing FPN [31] and FPN+FINE on Mask R-CNN R50 [13] trained on COCO (confidence threshold: 0.8).

5.4 Analysis

To better understand how mitigating semantic inconsistency improves detection performance, we analyze activation heatmaps and detection errors using Mask R-CNN R50 [13] trained with a $2\times$ schedule on COCO.

Activation Heatmap. Activation heatmaps are visualized in Figure 8. Taking the first row as an example, F_{high} concentrates activations on the airplane body, providing strong semantic cues but coarse spatial resolution, while F_{low} captures fine-grained boundaries but also activates background regions. Through cross-level interaction, the modulation map M re-weights object-relevant regions relative to the background. By applying residual modulation to preserve the spatial details of F_{low} , the resulting feature $F_{\text{low}}^{\text{aligned}}$ retains the sharp boundaries of the airplane while suppressing activations on background clutter.

Detection Error Analysis. We further investigate whether the refined activations produced by FINE translate into fewer detection errors. As shown in Table 5, a substantial 9.93% reduction in False Positives (FPs) yields a 5.71% gain in precision, while a 2.82% decrease in False Negatives (FNs) leads to a 1.52% increase in recall. Importantly, the FP reduction does not suppress foreground predictions, as the number of True Positives also increases (23,833 \rightarrow 24,186).

Consequently, the overall F1-score improves by 3.77%, confirming enhanced detection reliability. This improvement is further supported by qualitative results in Figure 9, where FPN produces spurious detections on background clutter such as complex textures and small structures, whereas FINE effectively suppresses these high-confidence FPs while preserving correct object predictions. Additional qualitative analyses are provided in Appendix Section G.

6 Conclusion

We propose Feature Interaction Network (FINE), a lightweight plug-and-play module that introduces alignment-aware cross-level attention into multi-scale feature fusion. Through Alignment-Aware Token Sampling, bottleneck multi-head cross-level attention, and residual spatial-channel modulation, FINE consistently improves detection accuracy with negligible computational overhead. These gains are primarily driven by a substantial reduction in false positives and marked improvements in small object detection, highlighting the importance of mitigating semantic inconsistency across pyramid levels in modern object detectors.

FINE currently operates within the conventional backbone–neck dichotomy, treating feature extraction and fusion as distinct stages. A promising future direction is to dissolve this boundary by embedding cross-scale attention directly throughout the feature extraction process, thereby unifying representation learning and multi-scale fusion into a single paradigm.

Appendix

A Training Setup

For our experiments, real-time object detectors (reported in Table 1) are trained using $4\times$ NVIDIA GeForce RTX 3090 GPUs, while classic object detectors are trained on $2\times$ NVIDIA RTX Ada 6000 GPUs. In all cases, we strictly adhere to the official training recipes and hyperparameters provided by the respective baseline implementations to ensure a fair and reproducible comparison.

B Downsampling Operator in Alignment-Aware Token Sampling

We present an ablation study on the downsampling operator $\text{Down}(\cdot)$ used within our Alignment-Aware Token Sampling (AATS) (Eq. 4), with results summarized in Table 6. Although a learnable operator such as depthwise separable convolution (DWConv) [5] could capture richer local statistics, parameter-free pooling operators (MaxPool and AvgPool) achieve comparable performance while introducing no additional parameters or computational overhead. This suggests that the primary role of $\text{Down}(\cdot)$ in AATS is not complex feature transformation, but rather the alignment of effective receptive fields across feature levels. Consequently, a simple pooling operator is sufficient to provide the required spatial aggregation for ERF alignment. Based on these results, we adopt average pooling as the default implementation of AATS due to its simplicity, parameter-free design, and smoother preservation of regional feature distributions compared to the discrete selection behavior of max pooling.

$\text{Down}(\cdot)$	MACs	#Params	AP
DWConv	2.46M	+6.14K	38.1
MaxPool	-	-	38.2
AvgPool	-	-	38.2

Table 6: Ablation on different downsampling operators in Alignment-Aware Token Sampling. Results are evaluated using Faster R-CNN R50 [45] on COCO val2017 ($1\times$ training schedule).

C Channel Dimension Unification

As described in Section 3, most FPN-based detectors unify the channel dimensions of hierarchical features before fusion, by applying 1×1 convolutions that

project each feature map $\{S_2, S_3, S_4\}$ into a common embedding space with C channels. This design simplifies subsequent fusion and attention operations, including those in our proposed FINE module, which assumes channel-consistent features. Therefore, no additional preprocessing is required for channel alignment in such architectures.

In contrast, the YOLO series [22, 23, 27, 49, 53] retains the original backbone output channels $\{C_2, C_3, C_4\}$ without enforcing channel uniformity across scales. To enable cross-level attention, the channel dimensions are aligned by projecting the high-level feature $S_{l+1} \in \mathbb{R}^{H_{l+1} \times W_{l+1} \times C_{l+1}}$ into the channel space of the low-level feature $S_l \in \mathbb{R}^{H_l \times W_l \times C_l}$ using a 1×1 convolution:

$$F_{\text{low}} = S_l, \quad F_{\text{high}} = \text{Conv}_{1 \times 1}(S_{l+1}) \quad (10)$$

where F_{low} is used directly without channel projection, and $F_{\text{high}} \in \mathbb{R}^{H_{l+1} \times W_{l+1} \times C_l}$ is the channel-adjusted high-level feature used in FINE. This lightweight embedding step is introduced only when required by the architecture, allowing FINE to remain broadly applicable across diverse detector architectures while preserving its feature alignment capability.

D Applicability to Dense Prediction Tasks

Although FINE is primarily evaluated for object detection, its core principle of enhancing semantic consistency across hierarchical features is also applicable to pixel-level dense prediction tasks. To demonstrate this generality, we integrate FINE into representative frameworks for instance, semantic, and panoptic segmentation. For instance segmentation, we follow the torchvision training recipe [51], while semantic and panoptic segmentation experiments adopt the $1 \times$ training schedule from OpenMMLab [41], using input resolutions of 640×640 for COCO [33] and 512×1024 for Cityscapes [6].

As shown in Table 7, FINE consistently improves performance across all three tasks with negligible computational overhead. For instance segmentation on COCO, adding FINE to Mask R-CNN R50 [13] improves box AP and mask AP by +1.8 and +0.9, respectively. For semantic segmentation on Cityscapes, incorporating FINE into Semantic FPN [24] yields a +1.9 mIoU improvement. For panoptic segmentation on COCO, Panoptic FPN with FINE achieves +0.7 gains in PQ (Panoptic Quality), SQ (Segmentation Quality), and RQ (Recognition Quality), following the evaluation metrics of [25].

These results demonstrate that although FINE extracts region-level semantic context due to its bottleneck architecture, the resulting feature representations are by no means coarse. By using this regional context to modulate high-resolution low-level features via a residual connection, FINE effectively broadcasts strong categorical cues to individual pixels while preserving fine-grained spatial details.

Instance segmentation on COCO [33] dataset						
Model	FINE	#Params	FLOPs	Box AP	Mask AP	
Mask R-CNN R50 [13]	–	44.4M	134.4G	37.9	34.6	
Mask R-CNN R50	✓	45.5M	135.5G	39.7 (+1.8)	35.5 (+0.9)	
Semantic segmentation on Cityscapes [6] dataset						
Model	FINE	#Params	FLOPs	mIoU		
Semantic FPN [24]	–	28.5M	90.9G	74.5		
Semantic FPN	✓	30.1M	91.7G	76.4 (+1.9)		
Panoptic segmentation on COCO dataset						
Model	FINE	#Params	FLOPs	PQ	SQ	RQ
Panoptic FPN [24]	–	46.0M	156.7G	40.2	77.8	49.3
Panoptic FPN	✓	47.6M	157.3G	40.9 (+0.7)	78.5 (+0.7)	50.0 (+0.7)

Table 7: Generality of FINE across dense prediction tasks. Beyond object detection, FINE consistently enhances performance in instance, semantic, and panoptic segmentation with minimal computational overhead.

Model	Fusion Method	FLOPs	AP ₅₀
YOLOv5-S [22]	PAN	37.5G	45.9
	PAN + FINE	40.8G	46.9 (+1.0)
YOLOv6-S v3.0 [27]	PAN	72.2G	44.8
	PAN + FINE	74.5G	45.6 (+0.8)
YOLOv8-S [23]	PAN	44.7G	46.3
	PAN + FINE	49.2G	47.2 (+0.9)

Table 8: Performance on VisDrone-DET2019. All models are evaluated with an input resolution of 800×800 .

E Performance on VisDrone Dataset

The VisDrone-DET2019 dataset [9] is a challenging benchmark characterized by crowded scenes, complex backgrounds, and a large proportion of small objects captured from aerial viewpoints. To evaluate the robustness of FINE under these demanding conditions, we integrate it into several representative real-time detectors [22, 23, 27]. As summarized in Table 8, integrating FINE consistently improves AP₅₀ across all evaluated detectors, yielding gains of up to +1.0.

Notably, these YOLO baselines are primarily designed for generic object detection and real-time efficiency rather than for specialized small-object detection. Nevertheless, FINE consistently improves detection accuracy with marginal computational overhead, demonstrating that selectively modulating low-level features under high-level semantic guidance effectively benefits target localization in small-object-dominated scenarios.

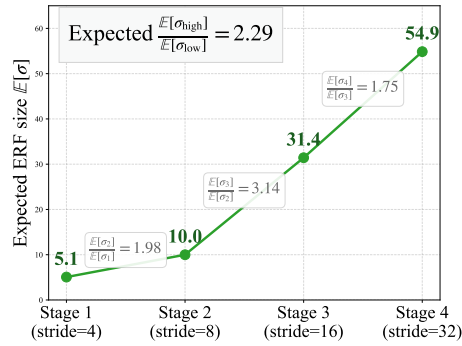


Fig. 10: Empirical analysis of effective receptive fields (ERFs) in ResNet-50 [14]. Evaluated over the COCO `val2017`, the average expected ERF expansion ratio across adjacent stages closely approximates the architectural stride ratio.

F Effective Receptive Field Analysis

Following the theoretical framework established in [39], we define the effective receptive field (ERF) of a feature activation $y_{i,j}$ at spatial location (i, j) by measuring its gradient-based influence with respect to all pixels on the input plane. Formally, for any input pixel $x_{u,v}$ at spatial coordinates (u, v) , the influence is defined as

$$g_{u,v} = \left| \frac{\partial y_{i,j}}{\partial x_{u,v}} \right|. \quad (11)$$

The ERF is characterized by the spatial distribution of $g_{u,v}$ across all input coordinates (u, v) . Under a cascade of convolutional layers, the central limit theorem implies that this distribution asymptotically approaches a 2D Gaussian:

$$g_{u,v} \propto \exp\left(-\frac{\|(u, v) - \boldsymbol{\mu}\|^2}{2\sigma^2}\right), \quad (12)$$

where $\boldsymbol{\mu} = (\mu_u, \mu_v)$ denotes the spatial center of the effective receptive field, and the standard deviation σ is taken as *the effective receptive field (ERF) size*, which approximates its spatial radius.

To empirically validate the relationship between ERF size [39] and network downsampling, we conduct an ERF analysis on ResNet-50 [14] over all 5,000 images of the COCO `val2017` split. For each image, we compute σ at the central spatial location of the final feature map within each backbone stage and average these values across the dataset to obtain $E[\sigma]$ per stage. As illustrated in Figure 10, the ratio of expected ERF sizes between adjacent stages closely approximates the architectural stride ratio:

$$\frac{E[\sigma_{\text{high}}]}{E[\sigma_{\text{low}}]} \approx s, \quad (13)$$

where s denotes the stride ratio between adjacent stages. Averaged across all adjacent stage pairs (Stage 1-2, 2-3, and 3-4), this ratio is 2.29. This closely matches the theoretical stride ratio of $s = 2$, providing an empirical justification for setting the alignment-aware sampling ratio to $r = 2$ in our Alignment-Aware Token Sampling strategy.

G Qualitative Analysis

False Negative Reduction. As quantitatively shown in Table 5, the simultaneous reduction in both False Positives (FPs) and False Negatives (FNs) indicates that FINE not only suppresses background clutter but also amplifies foreground object signals. As visualized in Figure 11, the baseline FPN frequently misses small or partially visible objects due to insufficient semantic abstraction in the low-level features. By enforcing semantic consistency across hierarchical levels, FINE recovers missed detections of small objects and those with low visual saliency (*e.g.*, snowboards, frisbees, skis, and stop signs) without compromising correct predictions made by the baseline.

Instance Segmentation. Figure 12 further demonstrates that the representational benefits of FINE extend to pixel-level instance segmentation. As highlighted in the red zoomed-in crops, the baseline FPN struggles with precise boundary localization, producing coarse masks that either bleed into the background (*e.g.*, mistakenly segmenting shadows around the teddy bear) or exhibit fragmented contours on complex shapes (*e.g.*, missing edges of the skateboard). By modulating low-level features with high-level semantic context, FINE alleviates these pixel-level ambiguities, enabling cleaner instance separation and sharper object boundaries.



Fig. 11: False negatives reduction comparing FPN [31] and FPN+FINE on Mask R-CNN R50 [13] trained on COCO (confidence threshold: 0.8).

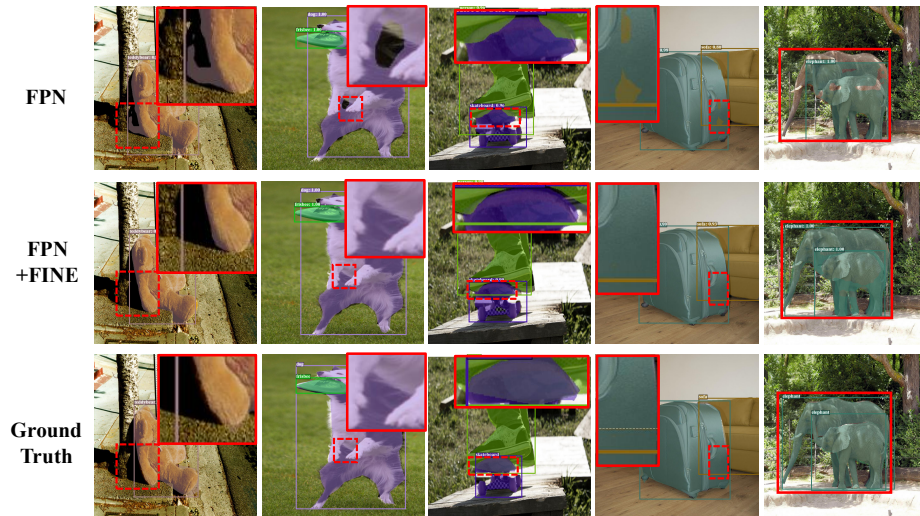


Fig. 12: Instance segmentation results comparing FPN [31] and FPN+FINE on Mask R-CNN R50 [13] trained on COCO. Red solid boxes show zoomed-in views of the dashed regions.

References

1. Bochkovskiy, A., Wang, C.Y., Liao, H.Y.M.: Yolov4: Optimal speed and accuracy of object detection. arXiv preprint arXiv:2004.10934 (2020)
2. Bolya, D., Fu, C.Y., Dai, X., Zhang, P., Feichtenhofer, C., Hoffman, J.: Token merging: Your ViT but faster. In: International Conference on Learning Representations (2023)
3. Cai, H., Li, J., Hu, M., Gan, C., Han, S.: Efficientvit: Lightweight multi-scale attention for high-resolution dense prediction. In: Proceedings of the IEEE/CVF international conference on computer vision. pp. 17302–17313 (2023)
4. Carion, N., Massa, F., Synnaeve, G., Usunier, N., Kirillov, A., Zagoruyko, S.: End-to-end object detection with transformers. In: European conference on computer vision. pp. 213–229. Springer (2020)
5. Chollet, F.: Xception: Deep learning with depthwise separable convolutions. In: Proceedings of the IEEE conference on computer vision and pattern recognition. pp. 1251–1258 (2017)
6. Cordts, M., Omran, M., Ramos, S., Rehfeld, T., Enzweiler, M., Benenson, R., Franke, U., Roth, S., Schiele, B.: The cityscapes dataset for semantic urban scene understanding. In: Proceedings of the IEEE conference on computer vision and pattern recognition. pp. 3213–3223 (2016)
7. Dai, Y., Gieseke, F., Oehmcke, S., Wu, Y., Barnard, K.: Attentional feature fusion. In: Proceedings of the IEEE/CVF winter conference on applications of computer vision. pp. 3560–3569 (2021)
8. Dosovitskiy, A., Beyer, L., Kolesnikov, A., Weissenborn, D., Zhai, X., Unterthiner, T., Dehghani, M., Minderer, M., Heigold, G., Gelly, S., et al.: An image is worth 16x16 words: Transformers for image recognition at scale. arXiv preprint arXiv:2010.11929 (2020)
9. Du, D., Zhu, P., Wen, L., Bian, X., Lin, H., Hu, Q., Peng, T., Zheng, J., Wang, X., Zhang, Y., et al.: Visdrone-det2019: The vision meets drone object detection in image challenge results. In: Proceedings of the IEEE/CVF international conference on computer vision workshops. pp. 0–0 (2019)
10. Ghiasi, G., Lin, T.Y., Le, Q.V.: Nas-fpn: Learning scalable feature pyramid architecture for object detection. In: Proceedings of the IEEE/CVF conference on computer vision and pattern recognition. pp. 7036–7045 (2019)
11. Gong, Y., Yu, X., Ding, Y., Peng, X., Zhao, J., Han, Z.: Effective fusion factor in fpn for tiny object detection. In: Proceedings of the IEEE/CVF winter conference on applications of computer vision. pp. 1160–1168 (2021)
12. Guo, C., Fan, B., Zhang, Q., Xiang, S., Pan, C.: Augfpn: Improving multi-scale feature learning for object detection. In: Proceedings of the IEEE/CVF conference on computer vision and pattern recognition. pp. 12595–12604 (2020)
13. He, K., Gkioxari, G., Dollár, P., Girshick, R.: Mask r-cnn. In: Proceedings of the IEEE international conference on computer vision. pp. 2961–2969 (2017)
14. He, K., Zhang, X., Ren, S., Sun, J.: Deep residual learning for image recognition. In: Proceedings of the IEEE conference on computer vision and pattern recognition. pp. 770–778 (2016)
15. Hu, J., Shen, L., Sun, G.: Squeeze-and-excitation networks. In: Proceedings of the IEEE conference on computer vision and pattern recognition. pp. 7132–7141 (2018)
16. Hu, M., Li, Y., Fang, L., Wang, S.: A2-fpn: Attention aggregation based feature pyramid network for instance segmentation. In: Proceedings of the IEEE/CVF conference on computer vision and pattern recognition. pp. 15343–15352 (2021)

17. Huang, J., Chen, Z., Wu, Q.J., Liu, C., Yuan, H., He, W.: Catfpn: Adaptive feature pyramid with scale-wise concatenation and self-attention. *IEEE Transactions on Circuits and Systems for Video Technology* **32**(12), 8142–8152 (2021)
18. Huang, S., Lu, Z., Cheng, R., He, C.: Fapn: Feature-aligned pyramid network for dense image prediction. In: *Proceedings of the IEEE/CVF international conference on computer vision*. pp. 864–873 (2021)
19. Huang, S., Lu, Z., Cun, X., Yu, Y., Zhou, X., Shen, X.: Deim: Detr with improved matching for fast convergence. In: *Proceedings of the computer vision and pattern recognition conference*. pp. 15162–15171 (2025)
20. Huang, Z., Wang, X., Huang, L., Huang, C., Wei, Y., Liu, W.: Ccnet: Criss-cross attention for semantic segmentation. In: *Proceedings of the IEEE/CVF International Conference on Computer Vision (ICCV)* (October 2019)
21. Huang, Z., Wei, Y., Wang, X., Liu, W., Huang, T.S., Shi, H.: Alignseg: Feature-aligned segmentation networks. *IEEE Transactions on Pattern Analysis and Machine Intelligence* **44**(1), 550–557 (2021)
22. Jocher, G.: YOLOv5 by Ultralytics (May 2020). <https://doi.org/10.5281/zenodo.3908559>, <https://github.com/ultralytics/yolov5>, aGPL-3.0 License
23. Jocher, G., Qiu, J., Chaurasia, A.: Ultralytics YOLO (Jan 2023), <https://github.com/ultralytics/ultralytics>
24. Kirillov, A., Girshick, R., He, K., Dollár, P.: Panoptic feature pyramid networks. In: *Proceedings of the IEEE/CVF conference on computer vision and pattern recognition*. pp. 6399–6408 (2019)
25. Kirillov, A., He, K., Girshick, R., Rother, C., Dollar, P.: Panoptic segmentation. In: *Proceedings of the IEEE/CVF Conference on Computer Vision and Pattern Recognition (CVPR)* (June 2019)
26. Koohpayegani, S.A., Pirsiavash, H.: Sima: Simple softmax-free attention for vision transformers. In: *Proceedings of the IEEE/CVF Winter Conference on Applications of Computer Vision*. pp. 2607–2617 (2024)
27. Li, C., Li, L., Geng, Y., Jiang, H., Cheng, M., Zhang, B., Ke, Z., Xu, X., Chu, X.: Yolov6 v3.0: A full-scale reloading. *arXiv preprint arXiv:2301.05586* (2023)
28. Li, F., Zhang, H., Liu, S., Guo, J., Ni, L.M., Zhang, L.: Dn-detr: Accelerate detr training by introducing query denoising. In: *Proceedings of the IEEE/CVF conference on computer vision and pattern recognition*. pp. 13619–13627 (2022)
29. Li, H.: Rethinking features-fused-pyramid-neck for object detection. In: *European Conference on Computer Vision*. pp. 74–90. Springer (2024)
30. Liang, Y., Ge, C., Tong, Z., Song, Y., Wang, J., Xie, P.: Not all patches are what you need: Expediting vision transformers via token reorganizations. In: *International Conference on Learning Representations* (2022), https://openreview.net/forum?id=BjyvwnXXVn_
31. Lin, T.Y., Dollár, P., Girshick, R., He, K., Hariharan, B., Belongie, S.: Feature pyramid networks for object detection. In: *Proceedings of the IEEE conference on computer vision and pattern recognition*. pp. 2117–2125 (2017)
32. Lin, T.Y., Goyal, P., Girshick, R., He, K., Dollár, P.: Focal loss for dense object detection. In: *Proceedings of the IEEE international conference on computer vision*. pp. 2980–2988 (2017)
33. Lin, T.Y., Maire, M., Belongie, S., Hays, J., Perona, P., Ramanan, D., Dollár, P., Zitnick, C.L.: Microsoft coco: Common objects in context. In: *Computer vision—ECCV 2014: 13th European conference, zurich, Switzerland, September 6–12, 2014, proceedings, part v 13*. pp. 740–755. Springer (2014)

34. Liu, S., Li, F., Zhang, H., Yang, X., Qi, X., Su, H., Zhu, J., Zhang, L.: DAB-DETR: Dynamic anchor boxes are better queries for DETR. In: International Conference on Learning Representations (2022), <https://openreview.net/forum?id=oMI9Pj0b9J1>
35. Liu, S., Qi, L., Qin, H., Shi, J., Jia, J.: Path aggregation network for instance segmentation. In: Proceedings of the IEEE conference on computer vision and pattern recognition. pp. 8759–8768 (2018)
36. Liu, Z., Lin, Y., Cao, Y., Hu, H., Wei, Y., Zhang, Z., Lin, S., Guo, B.: Swin transformer: Hierarchical vision transformer using shifted windows. In: Proceedings of the IEEE/CVF international conference on computer vision. pp. 10012–10022 (2021)
37. Lu, J., Yao, J., Zhang, J., Zhu, X., Xu, H., Gao, W., Xu, C., Xiang, T., Zhang, L.: Soft: Softmax-free transformer with linear complexity. *Advances in Neural Information Processing Systems* **34**, 21297–21309 (2021)
38. Lu, L., Xiao, Y., Chang, X., Wang, X., Ren, P., Ren, Z.: Deformable attention-oriented feature pyramid network for semantic segmentation. *Knowledge-Based Systems* **254**, 109623 (2022)
39. Luo, W., Li, Y., Urtasun, R., Zemel, R.: Understanding the effective receptive field in deep convolutional neural networks. *Advances in neural information processing systems* **29** (2016)
40. Mehta, S., Rastegari, M.: Mobilevit: light-weight, general-purpose, and mobile-friendly vision transformer. arXiv preprint arXiv:2110.02178 (2021)
41. MMSegmentation Contributors: OpenMMLab Semantic Segmentation Toolbox and Benchmark (Jul 2020), <https://github.com/open-mmlab/mms Segmentation>
42. NVIDIA: Tensorrt. <https://github.com/NVIDIA/TensorRT> (2024), gitHub repository
43. Peng, Y., Li, H., Wu, P., Zhang, Y., Sun, X., Wu, F.: D-fine: Redefine regression task in detr as fine-grained distribution refinement. arXiv preprint arXiv:2410.13842 (2024)
44. Rao, Y., Zhao, W., Liu, B., Lu, J., Zhou, J., Hsieh, C.J.: Dynamicvit: Efficient vision transformers with dynamic token sparsification. In: *Advances in Neural Information Processing Systems (NeurIPS)* (2021)
45. Ren, S., He, K., Girshick, R., Sun, J.: Faster r-cnn: Towards real-time object detection with region proposal networks. *Advances in neural information processing systems* **28** (2015)
46. Ronneberger, O., Fischer, P., Brox, T.: U-net: Convolutional networks for biomedical image segmentation. In: *International Conference on Medical image computing and computer-assisted intervention*. pp. 234–241. Springer (2015)
47. Tan, M., Pang, R., Le, Q.V.: Efficientdet: Scalable and efficient object detection. In: *Proceedings of the IEEE/CVF conference on computer vision and pattern recognition*. pp. 10781–10790 (2020)
48. Tang, L., Li, B.: Class: cross-level attention and supervision for salient objects detection. In: *Proceedings of the Asian Conference on Computer Vision* (2020)
49. Tian, Y., Ye, Q., Doermann, D.: Yolov12: Attention-centric real-time object detectors. In: *Advances in Neural Information Processing Systems* (2025)
50. Tian, Z., Shen, C., Chen, H., He, T.: Fcos: Fully convolutional one-stage object detection. In: *Proceedings of the IEEE/CVF international conference on computer vision*. pp. 9627–9636 (2019)
51. TorchVision: TorchVision: PyTorch’s Computer Vision library (Nov 2025), <https://github.com/pytorch/vision>

52. Vaswani, A., Shazeer, N., Parmar, N., Uszkoreit, J., Jones, L., Gomez, A.N., Kaiser, L., Polosukhin, I.: Attention is all you need. *Advances in neural information processing systems* **30** (2017)
53. Wang, A., Chen, H., Liu, L., Chen, K., Lin, Z., Han, J., et al.: Yolov10: Real-time end-to-end object detection. *Advances in neural information processing systems* **37**, 107984–108011 (2024)
54. Wang, C., Zhong, C.: Adaptive feature pyramid networks for object detection. *IEEE Access* **9**, 107024–107032 (2021). <https://doi.org/10.1109/ACCESS.2021.3100369>
55. Wang, S., Xia, C., Lv, F., Shi, Y.: Rt-detr3: real-time end-to-end object detection with hierarchical dense positive supervision. In: *2025 IEEE/CVF Winter Conference on Applications of Computer Vision (WACV)*. pp. 1628–1636. IEEE (2025)
56. Wu, H., Xiao, B., Codella, N., Liu, M., Dai, X., Yuan, L., Zhang, L.: Cvt: Introducing convolutions to vision transformers. In: *Proceedings of the IEEE/CVF international conference on computer vision*. pp. 22–31 (2021)
57. Zhang, D., Zhang, H., Tang, J., Wang, M., Hua, X., Sun, Q.: Feature pyramid transformer. In: *Computer Vision–ECCV 2020: 16th European Conference, Glasgow, UK, August 23–28, 2020, Proceedings, Part XXVIII 16*. pp. 323–339. Springer (2020)
58. Zhao, Y., Lv, W., Xu, S., Wei, J., Wang, G., Dang, Q., Liu, Y., Chen, J.: Detsr beat yolos on real-time object detection. In: *Proceedings of the IEEE/CVF conference on computer vision and pattern recognition*. pp. 16965–16974 (2024)
59. Zhu, X., Su, W., Lu, L., Li, B., Wang, X., Dai, J.: Deformable detr: Deformable transformers for end-to-end object detection. *arXiv preprint arXiv:2010.04159* (2020)